Physica Medica 59 (2019) 92–99

Contents lists available at ScienceDirect

Physica Medica

journal homepage: www.elsevier.com/locate/ejmp

Original paper

Analytical simulator of proton radiography and tomography for different detector configurations

Chiara Gianoli[a,*], Sebastian Meyer[a], Lorena Magallanes[a,b], Chiara Paganelli[c], Guido Baroni[c], Katia Parodi[a]

[a] Faculty of Physics, Department of Medical Physics, Experimental Physics, Ludwig-Maximilians-Universität München, Munich, Germany
[b] Heidelberg Ion Beam Therapy Center, Heidelberg University Hospital, Heidelberg, Germany
[c] Dipartimento di Elettronica, Informazione e Bioingegneria (DEIB), Politecnico di Milano, Milano, Italy

ARTICLE INFO

Keywords:
Proton radiography and tomography
Analytical simulator
List-mode and integration-mode detector configurations
Most Likely Path algorithm

ABSTRACT

Purpose: An analytical simulator of ion Radiography (iRad) and Computed Tomography (iCT) for protons is proposed to serve as imaging benchmark for different detector configurations.
Methods: The analytical simulator is applied to an anthropomorphic phantom and provides iRad and iCT benchmarks. Proton trajectories are traced relying on the Most Likely Path (MLP) algorithm. To simulate the proton trajectories the Multiple Coulomb Scattering (MCS) model embedded in the MLP algorithm is extended to non-uniform water equivalent materials according to variable substitution in the well-known statistical description in uniform water. The proton trajectories are instead estimated relying on the typical assumption of uniform water, thus causing intrinsic inaccuracies of the MLP algorithm. In this work the analytical simulator is used to explore and firstly compare the imaging performances of list-mode and integration-mode detector configurations with proton pencil beam scanning.
Results: The intrinsic inaccuracies of the MLP algorithm affect the imaging performances of list-mode detector configuration, which nevertheless remains superior to integration-mode detector configuration for iCTs. For relatively higher proton statistics, comparable or better imaging performances are offered by integration-mode detector configuration for iRads (upto 29.2% of WET difference). Uncertainties of proton trajectories due to beam spot size are shown to compromise the imaging performances of integration-mode detector configuration, but also to affect the accuracy of the MLP algorithm for list-mode detector configuration.
Conclusions: Based on MCS model in non-uniform water equivalent materials, the proposed simulation environment can serve for development and testing of dedicated imaging methodologies prior to and in combination with realistic Monte Carlo simulations.

1. Introduction

Compared to photon beam therapy, ion beam therapy enables improved targeting of the therapeutic dose to the tumor, relying on the Bragg peak [1,2]. Full clinical exploitation of the physical and biological advantages offered by ion beam therapy is still challenged by underlying inaccuracies in treatment planning and delivery, especially due to uncertainties in the used patient model. These planning uncertainties mainly relate to conversion of the X-ray Computed Tomography (CT) image, expressed as relative photon linear attenuation coefficients in Hounsfield Units (HU), into the ion stopping power relative to water, or the relative Water Equivalent Path Length (rWEPL) [3,4]. Additional delivery uncertainties are due to inter- and intra-fractional anatomical changes occurring during the course of the treatment [5,6].

Radiographic and tomographic ion imaging [7–9], or ion Radiography (iRad) and ion Computed Tomography (iCT) respectively, are increasingly emerging research concepts in ion beam therapy [10–12]. Their rationale relies on the information retrieved by highly energetic ions that completely traverse the object of interest. An iRad provides the Water Equivalent Thickness (WET) of the object of interest relying on the approximate energy independence of the stopping power ratios in the energetic regimes of interest [13]. Extending the use of multiple iRads acquired by either rotating the object of interest or the beam delivery system for tomographic acquisition, the iCT image can be reconstructed as spatial distribution of rWEPLs, thus basically eluding the

* Corresponding author at: Am Coulombwall 1, 85748 Garching bei München, Germany.
E-mail address: chiara.gianoli@physik.uni-muenchen.de (C. Gianoli).

https://doi.org/10.1016/j.ejmp.2019.03.002
Received 23 September 2018; Received in revised form 8 February 2019; Accepted 4 March 2019
Available online 08 March 2019

uncertainties inherent in the conversion of X-ray CT image into rWEPL.

The detector configuration originally designed for iCT imaging is composed of a total absorption detector (i.e., a calorimeter) to measure the residual energy of each individual ion and a synchronized tracking system [14–20]. The tracking system consists of two pairs of thin silicon detector layers placed prior (entrance position) and posterior (exit position) to the object of interest in order to measure position and angle of the ion. Thus, such a detector configuration is defined as "list-mode". Simplified configurations are derived by removing the tracking system [21] with advantages in terms of realization costs and clinical implementation. In pencil beam scanning these detector configurations are typically defined as "integration-mode", as the residual energy measurement is carried out for the ion ensemble of each pencil beam. In particular, the total absorption detector can be discretized into a stack of absorbers interleaved with detector layers to obtain a discrete Bragg peak signal, thus retrieving the ion range instead of the residual energy [14,22]. This integration-mode detector configuration has been initially explored in the research context of carbon ion beam therapy. Ambiguities in range signals occur in the presence of material heterogeneities within the object of interest. For protons, these ambiguities increase due to larger Beam Spot Size (BSS) and Multiple Coulomb Scattering (MCS). Prior knowledge of the Bragg peak shape enables the application of signal processing methodologies capable of decomposing the signal into a linear combination of pristine Bragg peaks, thus recovering the individual WET components as a WET histogram [23]. Based on decomposition and in the presence of overlapping pencil beams due to BSS and MCS, the spatial information of WET components can be partially recovered to compensate for the loss of spatial resolution in the integration-mode detector configuration. These signal processing methodologies, adapting the WET histogram of each pencil beam based on anatomical priors [24] or working on the WET histogram of a neighborhood of pencil beams [25] have paved the way towards exploration of the integration-mode detector configuration in the research context of proton beam therapy. However, no comparative investigations with respect to the list-mode detector configuration for protons have been performed yet.

The technology developments in iRad and iCT are calling for dedicated imaging methodologies to make the most of the available information acquired with the selected detector configuration [26]. With the integration-mode detector configuration, tomographic image reconstruction relies on an imaging system model based on straight integration lines [23,27]. Although this is justified for carbon ions, algorithms have been specifically developed for protons to estimate the curved proton trajectory [28,29]. With the list-mode detector configuration, an estimation of the proton trajectory in uniform water is given by the Most Likely Path (MLP) algorithm, which is based on the inclusion of the Fermi-Eyges MCS model in the Bayes' formalism [30,31,32]. In principle, the MLP algorithm can be provided with MCS model extended to uniform water equivalent materials (water with uniform rWEPL different from one) and, when priors about heterogeneities are available, to non-uniform water equivalent materials (water with non-uniform rWEPLs different from one). However, the traversed object of interest is typically assumed to be uniform water and imaging methodologies are not extended either to uniform or non-uniform water equivalent materials. Conversely, the extension to materials non-equivalent to water requires a detailed physical characterization in terms of density and elemental composition of the object of interest [33].

In this work we firstly extend the MCS model embedded in the MLP algorithm to non-uniform water equivalent materials according to variable substitution in the well-known statistical description in uniform water. Secondly, we propose the so called PiRadAS or Proton imaging (Radiographic and Tomographic) Analytical Simulator, an analytical simulator of proton iRad and iCT to enable the development and testing of imaging methodologies [34]. The analytical simulator relies on the MLP algorithm provided with the MCS model extended to non-uniform water equivalent materials of the iCT reference. Finally, we make use of PiRadAS to compare the imaging performances of list-mode and integration-mode detector configurations, the latter enabled with a decomposition of the Bragg peak signal, with proton pencil beam scanning.

2. Material and methods

2.1. The imaging system model

In this work, PiRadAS is applied to the anthropomorphic non-uniform rational B-spline cardiac and torso (NCAT) phantom, version 2.0.2 [35]. The phantom represents the human anatomy and allows to model anatomical changes due to breathing and heart beating. Firstly, the photon linear attenuation coefficients of the phantom are linearly converted to HU and secondly to rWEPL, relying on realistic piecewise-linear calibration curves. The tomographic domain is parameterized in (x, y, z) with z representing the rotational axis of the imaging system. For each z, the projection lines are defined as $\rho = x\cos\theta + y\sin\theta$, where θ is the projection angle, while the integration lines are defined as $\delta = y\cos\theta - x\sin\theta$, and thus perpendicular to the projection line. The pencil beam position is therefore identified by (ρ, z) in the radiographic domain (i.e., the sinogram), which is therefore parameterized in (ρ, z, θ). The iCT reference in the tomographic domain is the spatial distribution of rWEPLs, directly given as input to the PiRadAS in order to describe the object of interest. The iRad reference in the radiographic domain is calculated as:

$$WET(\rho, z, \theta) = \varepsilon \sum_{\delta=1}^{D} rWEPL(\rho\cos\theta - \delta\sin\theta, \delta\cos\theta + \rho\sin\theta, z) = \varepsilon \sum_{\delta=1}^{D} rWEPL(\delta, \rho, z, \theta)$$

where $\delta = \{1, \cdots, D\}$ is the discretization index of the integration line. Both radiographic and tomographic domains are discretized by the pencil beam binning ε, which represents the voxel size of the tomographic domain and the pixel size of the radiographic domain, respectively. The geometrical and physical parameters of the analytical simulations based on PiRadAS are detailed in Table 1, with respect to the parameters of an original PiRadAS. The original PiRadAS is provided with proton statistics that are able to cover, entirely or partially, the voxel of the tomographic domain (for the given geometrical

Table 1
The geometrical and physical parameters of PiRadAS. The parameters adopted for the original PiRadAS are specified in bold.

Geometry		
Radiography sampling	Isotropic size of the pencil beam binning, ε (cm)	{**0.30**; 0.15}
	Number of bins along ρ, N_ρ	{**128**; 256}
	Number of bins along z, N_z	{**100**; 200}
Tomography sampling	Size of the angular step in θ, $\Delta\theta$ (°)	{2.0; **1.0**; 0.5}
	Number of the angular steps in θ, N_θ	{**180**; 360}
Physics		
Beam energy	Energy of the pencil beam, E_p (MeV)	{**280**; 300}
Proton statistics	Number of proton trajectories per pencil beam, N_p	{**100**,75,50,25,20,15,10,5,3,1}
Beam spot size	Standard deviation of the BSS, σ_{BSS} (cm)	{**0.0** (i.e., ideal pencil beam), 0.3; 0.6}

parameters). Since this number is progressively reduced (Table 1), the number of proton trajectories of the original PiRadAS can be regarded as relatively high proton statistics.

2.2. The MCS model in non-uniform water equivalent materials

Firstly, the MCS model in uniform water is translated into the discrete form (see description in supplementary material). Secondly, the MCS model is extended to non-uniform water equivalent materials. In particular, the physical characterization of water in terms of density and elemental composition is maintained, whereas the discretization index δ adopted for the MCS model in uniform water is replaced according to variable substitution by the water equivalent cumulative vector $\delta_{we} = \{\sum_{\delta=1}^{1} rWEPL(\delta, \rho, z, \theta), \cdots, \sum_{\delta=1}^{D} rWEPL(\delta, \rho, z, \theta)\}$, with $\varepsilon\delta_{we}(D) = WET(\rho, z, \theta)$. The variances of the bivariate Gaussian distribution ${\sigma_{tMCS_{we}}}^2$ and ${\sigma_{t\varphi_{MCS_{we}}}}^2$ are therefore expressed as:

$$\sigma_{tMCS_{we}}(\rho, z, \theta)^2 = E_0^2\left(1 + 0.038ln\left(\frac{\varepsilon\delta_{we}(D)}{X_{(H_2O)}}\right)\right)^2 \sum_{\delta=1}^{D}\left(\frac{(\varepsilon\delta_{we}(D) - \varepsilon\delta_{we}(\delta))^2}{X_{(H_2O)}\beta^2(\delta_{we}(\delta))p^2(\delta_{we}(\delta))}\right)r WEPL(\delta, \rho, z, \theta)\varepsilon$$

and

$$WET_p(\rho, z, \theta) = \varepsilon\sum_{\delta=1}^{D} rWEPL((\rho + t_{\rho_{MLP}})cos\theta - \delta sin\theta, \delta cos\theta + (\rho + t_{\rho_{MLP}})sin\theta, z + t_{zMLP})$$

$$\sigma_{t\varphi_{MCS_{we}}}(\rho, z, \theta)^2 = E_0^2\left(1 + 0.038ln\left(\frac{\varepsilon\delta_{we}(D)}{X_{(H_2O)}}\right)\right)^2 \sum_{\delta=1}^{D}\left(\frac{\varepsilon}{X_{(H_2O)}\beta^2(\delta_{we}(\delta))p^2(\delta_{we}(\delta))}\right)r WEPL(\delta, \rho, z, \theta)\varepsilon$$

Both the MCS models in uniform water and in non-uniform water equivalent materials are validated with respect to Monte Carlo (MC) simulations. Relying on the FLUKA platform [23,36,37], the water equivalent materials are obtained by scaling the density for charged particle ionization processes in water (excluding both elastic and inelastic nuclear interactions). Ideal pencil beams (annulled BSS) composed of 10^6 protons are simulated at 280 MeV and 300 MeV in 20 cm^3 uniform water with differently scaled mass density, and scored at 20 cm depth. The density is scaled by 0.6 and 1.4. Moreover, a total of 2480 ideal pencil beams each composed of 10^6 protons are simulated at aforementioned energies in the non-uniform water equivalent materials defined by integration lines of the anthropomorphic phantom with approximately 20 cm length (± 1 voxel). A bivariate Gaussian fitting is applied to the distribution of position and angle deviations. The difference between fitted (from MC simulations) and analytically calculated standard deviations is quantified. Accuracy and precision of the MCS model in non-uniform water equivalent materials with respect to MC simulations are then expressed as median value and interquartile range among the integration lines of the anthropomorphic phantom.

2.3. Simulation of the proton trajectory in non-uniform water equivalent materials

The proton trajectory deviates along the integration line δ from the pencil beam position (ρ, z) due to MCS and BSS. A (constant) standard deviation σ_{BSS} describes the Gaussian distribution due to BSS in air whereas the standard deviations $\sigma_{tMCS_{we}}$ and $\sigma_{t\varphi_{MCS_{we}}}$ describe the bivariate Gaussian distribution of position and angle deviations t and $t\varphi$ due to MCS in non-uniform water equivalent materials. The bivariate Gaussian distribution accounting for both MCS and BSS at the exit position of the object of interest is calculated according to the convolution of $\sigma_{tMCS_{we}}$ with σ_{BSS}, thus leading to $\sigma_{tMCS_{we}+BSS}$. The selection of the entrance and exit position deviations is based on a uniform random sampling of a standard Gaussian distribution (i.e., with zero mean and unit standard deviation), with a number of samples coinciding with the proton statistics of the pencil beam. These samples are then multiplied by the standard deviation $\sigma_{tMCS_{we}+BSS}$, thus obtaining the position deviations (t_ρ, t_z). The most probable angle deviations $(t\varphi_\rho, t\varphi_z)$ are then calculated as:

$$\begin{cases} t\varphi_\rho = t_\rho \frac{\sigma_{t\varphi_{MCS_{we}}}}{\sigma_{tMCS_{we}+BSS}} \\ t\varphi_z = t_z \frac{\sigma_{t\varphi_{MCS_{we}}}}{\sigma_{tMCS_{we}+BSS}} \end{cases}$$

thus resulting in linear functions of the position deviations. The simulation of the proton trajectories relies on the MCS model in non-uniform water equivalent materials embedded in the MLP algorithm (see description in supplementary material). The simulated proton trajectory is therefore defined as $(t_{\rho_{MLP_{we}}}, t_{zMLP_{we}})$ and is traced as unitary voxels centered in $(t_{\rho_{MLP_{we}}}, t_{zMLP_{we}})$.

2.4. List-mode and integration-mode detector configurations

The WET components in the radiographic domain of each pencil beam are analytically calculated by integrating the iCT reference along the traced trajectories $(t_{\rho_{MLP_{we}}}, t_{zMLP_{we}})$ as:

where $p = \{1, \cdots, N_p\}$ is the proton index.

In the list-mode detector configuration the WET components $WET_p(\rho, z, \theta)$ are stored independently for each proton of the pencil beam. Therefore, a 4D sinogram, parameterized in (ρ, z, θ, p) is obtained.

In the integration-mode detector configuration the WET components $WET_p(\rho, z, \theta)$ are instead stored as a histogram for the proton ensemble of each pencil beam (i.e., the WET histogram of the WET components). Therefore, a 4D sinogram, parameterized in (ρ, z, θ, s) is obtained, where s corresponds to the discretization index for the stacks of the total absorption detector. The discretization defining the number of WET components of the WET histogram is set to 179 discretization indexes, slightly larger than the maximum integer WET of the iRad reference (46 cm). Consequently, the WET histogram is obtained using the decomposition of the signal in a linear combination of pristine Bragg peak signals. Hence, the WET component with maximum occurrence can be selected as WET_{max} along the integration line. Alternatively, the WET components, weighted for the corresponding occurrences, are averaged to obtain the WET_{mean} along the integration line.

2.5. Tomographic image reconstruction

The tomographic image reconstruction relies on the Simultaneous Algebraic Reconstruction Technique (SART), which is considered state-of-the-art for transmission tomographic reconstruction [38]. In fact, the SART reconstruction is feasible even with a limited number of projections due to dosimetric and/or geometrical constraints, where the continuity of image and projection functions is not guaranteed. Different system matrices are implemented for list-mode and integration-mode detector configurations. The system matrix for the list-mode detector configuration requires estimation of proton trajectories relying on the MCS model in uniform water embedded in the MLP algorithm (*see* description in supplementary material). The estimated proton trajectory is therefore defined as $(t_{\rho_{MLP}}, t_{zMLP})$ and, similarly for $(t_{\rho_{MLP_{we}}}, t_{zMLP_{we}})$, is traced as unitary voxels centered in $(t_{\rho_{MLP}}, t_{zMLP})$.

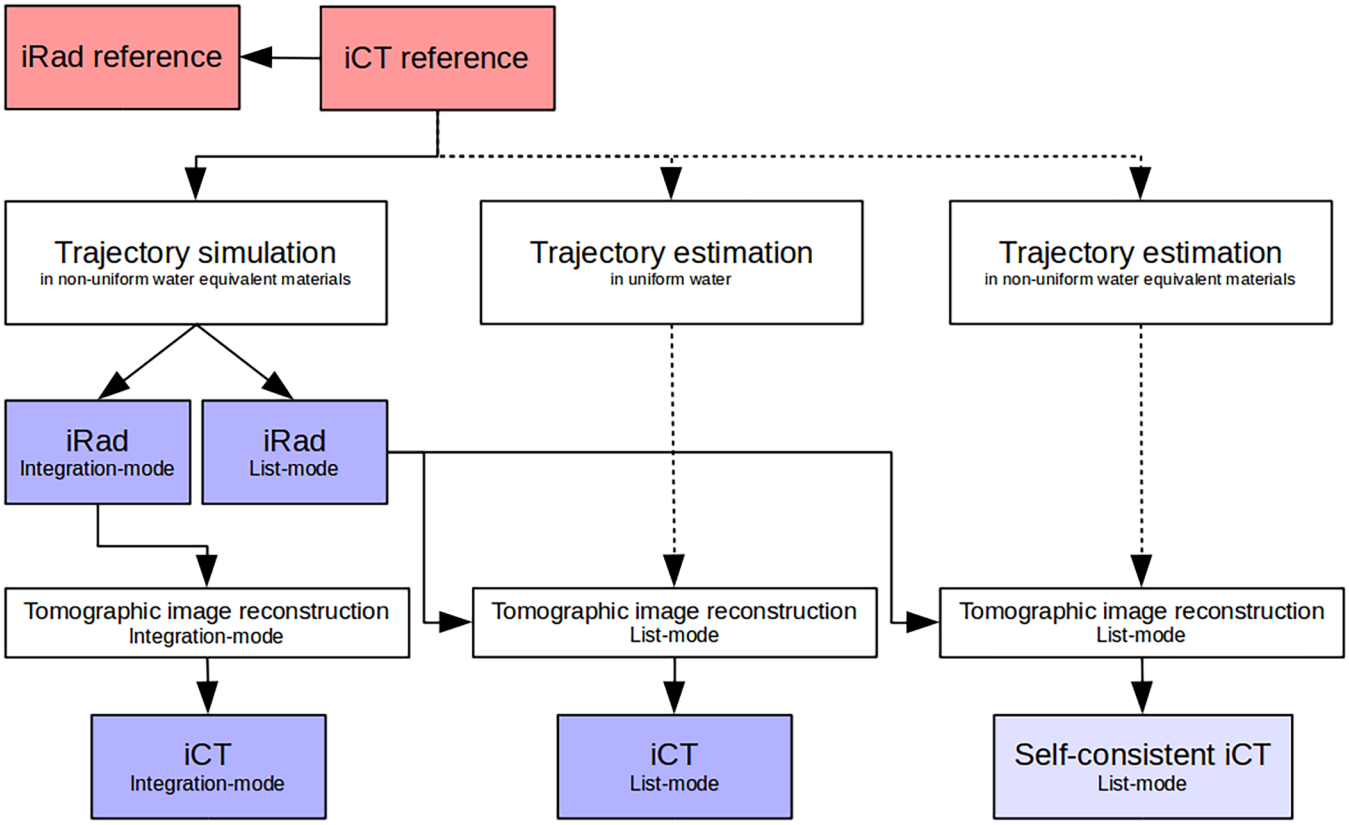

Fig. 1. Schematic representation of the analytical simulator for proton iRad and iCT. Tomographic image reconstruction for the list-mode detector configuration requires estimation of proton trajectories (dashed lines).

The intrinsic inaccuracies of the MLP algorithm, related to simulating the proton trajectories in non-uniform water equivalent materials and estimating them in uniform water, determine the ill-posed nature of tomographic image reconstruction in iCT imaging. The self-consistent reconstruction makes the estimation consistent with the simulation by using the simulated proton trajectories directly as estimation. In other words, the imaging system model is used for both simulation and estimation, thus excluding the intrinsic inaccuracy of the MLP algorithm. The proton trajectories are traced only within the object of interest relying on prior knowledge about edges of the object of interest. Conversely, the system matrix for the integration-mode reconstruction is a geometrical system matrix, thus treating the integration line as a trajectory. For a valid comparison, the same priors used for the list-mode detector configuration are adopted and outside the object of interest no lines are traced.

A schematic representation of the analytical simulator for proton iRad and iCT is displayed in Fig. 1.

2.6. Quantitative analysis

The imaging performances of the list-mode detector configuration, including self-consistent reconstruction, are compared to the imaging performances of the integration-mode detector configuration. The influence on imaging performances of the physical and geometrical parameters reported in Table 1 is explored. The following quantifications of imaging performances are assessed in both radiographic and tomographic domains in terms of:

- Difference of WET (radiographic domain) and rWEPL (tomographic domain) to iRad and iCT references, respectively, to globally quantify and statistically analyze the performance.
- Median value and interquartile range of the rWEPL difference to iCT reference within anatomical regions of interest of the anthropomorphic phantom to locally quantify the performance: heart, liver, lung lesion and lung [39].
- Spatial resolution of the lung lesion (i.e. lung as background), quantified at the 10% of the Modulation Transfer Function (MTF) [40].

3. Results

3.1. Validation of the MCS model in non-uniform water equivalent materials

The quantification of the MCS models in uniform water and in uniform and non-uniform water equivalent materials with respect to MC simulations is provided in Table 2.

The disagreement of the MCS model in uniform water with respect to MC simulations is compatible with the adjustability of the formula due to corrections or constant refinements (*see* description in supplementary material). The disagreement is consistent in the extension of the same MCS model to uniform and non-uniform water equivalent materials. Particularly, precision and accuracy of the MCS models result adequate for the proposed analytical simulator (fractions of the voxel size and the angular step).

3.2. Comparison of imaging performances of list-mode and integration-mode detector configurations

The number of iterations for the tomographic image reconstruction based on SART relies on the typical trade-off between convergence and noise break-up for the anatomical regions of interest [41]. The tomographic image reconstruction converges at iteration numbers about one hundred. The variation in subsequent iterations of the median value

Table 2
Difference between fitted and calculated standard deviations of the Gaussian distributions describing position and angle deviations for different density scaling of the water and the median value (m) and interquartile range (iqr) of the same quantification for the integration lines of the anthropomorphic phantom.

	Uniform water		Uniform water equivalent materials				Non-uniform water equivalent materials			
	1		0.6		1.4					
	position (mm)	angle (crad)	position (mm)	angle (crad)	position (mm)	angle (crad)	position (mm)		angle (crad)	
							m	iqr	m	iqr
280 MeV	0.43	0.39	−0.19	−0.21	0.96	1.00	0.39	0.18	0.43	0.02
300 MeV	0.40	0.38	−0.16	−0.20	0.91	0.92	0.38	0.17	0.40	0.02

Table 3
Median value (m) and interquartile range (iqr) of the rWEPL difference for list-mode and integration-mode detector configurations, for proton statistics equal to 100 protons, in comparison to self-consistent reconstruction.

					self-consistent		PiRadAS					
					list-mode		list-mode		integration-mode (WET_{max})		integration-mode (WET_{mean})	
					m	iqr	m	iqr	m	iqr	m	iqr
E_p 280 MeV	σ_{BSS} 0.0 cm	WET (mm)	global		–	–	−2.15	2.62	−1.53	2.62	−2.16	2.65
		rWEPL (-10^{-2})	global		0.04	1.24	0.03	2.37	−0.21	5.25	−0.42	4.38
			local	heart	0.33	1.70	0.12	2.33	−0.51	5.25	−0.48	4.16
				liver	0.08	0.37	0.02	1.26	−0.20	4.52	−0.37	3.26
				lung lesion	−5.39	20.48	−3.61	20.56	−3.64	19.90	−5.36	19.62
				lung	0.12	1.38	0.25	2.94	0.03	4.04	0.40	3.27
E_p 300 MeV	σ_{BSS} 0.0 cm	WET (mm)	global		–	–	−1.98	2.32	−1.40	2.39	−1.99	2.36
		rWEPL (-10^{-2})	global		0.04	1.19	0.08	2.33	−0.06	5.08	−0.25	4.26
			local	heart	0.29	1.65	0.09	3.47	−0.35	5.06	−0.35	4.21
				liver	0.07	0.37	0.03	0.41	−0.06	4.28	−0.24	3.08
				lung lesion	−5.39	20.64	−1.48	21.73	−4.07	20.36	−5.40	20.28
				lung	0.15	1.36	0.67	4.06	0.10	4.05	0.50	3.41
E_p 280 MeV	σ_{BSS} 0.3 cm	WET (mm)	global		–	–	−3.54	5.27	−1.74	3.69	−3.55	5.28
		rWEPL (-10^{-2})	global		−0.01	1.08	0.07	2.22	−0.45	8.87	−0.13	7.64
			local	heart	0.10	1.32	−0.01	1.70	−0.29	9.60	−1.10	7.66
				liver	−0.03	0.41	−0.26	1.28	−0.19	7.22	0.02	5.68
				lung lesion	−7.87	23.64	−8.30	23.19	−7.45	29.64	−25.98	23.73
				lung	−0.09	1.45	−0.02	2.28	−0.26	8.06	2.53	8.11

Table 4
Spatial resolution (mm) for list-mode and integration-mode detector configurations, for proton statistics equal to 100 protons, in comparison to self-consistent reconstruction.

		self-consistent	PiRadAS		
		list-mode	list-mode	integration-mode (WET_{max})	integration-mode (WET_{mean})
		Spatial resolution (mm)			
E_p 280 MeV	σ_{BSS} 0.0 cm	2.91	3.11	2.58	3.09
E_p 300 MeV	σ_{BSS} 0.0 cm	3.08	3.06	2.68	3.09
E_p 280 MeV	σ_{BSS} 0.3 cm	3.29	3.38	3.44	4.17

and interquartile range of the rWEPL difference is at most of order 10^{-3}, also for the lung lesion, for both list-mode and integration-mode detector configurations, in all analytical simulations. The number of iterations is therefore set equal to 100.

The comparison of the imaging performances in selected analytical simulations, quantified as WET difference, rWEPL difference and spatial resolution, for list-mode and integration-mode detector configurations, for proton statistics equal to 100 protons, is reported in Tables 3 and 4. Median values of WET difference are approximately the same order of magnitude as the interquartile ranges. In the radiographic domain, the list-mode detector configuration performs worse than the integration-mode detector configuration based on WET_{max} (29.2% of WET difference) but comparable to the integration-mode detector configuration based on WET_{mean} (1.4% of WET difference). In the integration-mode configuration based on WET_{max}, the selection of the WET component with the maximum occurrence favours the straighter proton trajectories [42], thus leading to sharp interfaces in the radiographic domain. For this reason, spatial resolution in the radiographic domain cannot be quantified in terms of blurring, such as a Point Spread Function or MTF. Median values of rWEPL difference are approximately one order of magnitude smaller than interquartile ranges. Smaller interquartile ranges of rWEPL difference are observed for the self-consistent reconstruction. In the tomographic domain, the list-mode detector configuration performs slightly better than the integration-mode detector configuration, except for lung lesion. For the integration-mode detector configuration based on WET_{max} the lung lesion has lower median value and interquartile ranges of rWEPL difference and better spatial resolution (though comparable to the voxel size). The spatial resolution expresses partial volume effects at the interfaces between lung and lung lesion. The partial volume effects are better compensated due to the assignment of the WET component with the maximum occurrence to the straight proton trajectory during tomographic image reconstruction. Hence, partial volume effects at anatomical interfaces in the tomographic domain differ from those in list-mode configuration and integration-mode configuration based on WET_{mean}. For the list-mode detector configuration, the maximum (absolute) difference between the simulated and estimated proton trajectories, quantifying the intrinsic inaccuracies of the MLP algorithm, is 0.32 cm for 280 MeV pencil beams. The larger errors occur along trajectories traversing larger heterogeneities, determining inhomogeneous inaccuracies in the list-mode detector configuration [43], which are seen to be appreciable in Fig. 2.

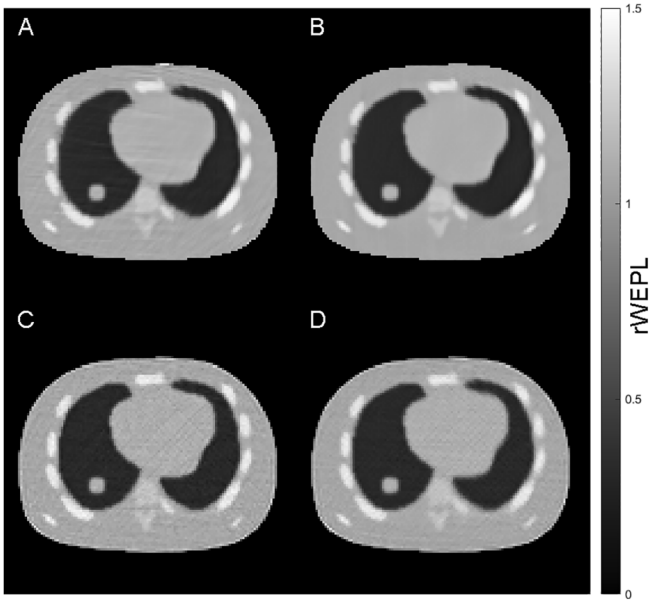

Fig. 2. Imaging performances of list-mode (A), self-consistent reconstruction (B), and integration-mode detector configurations, based on WET_{max} (C) and based on WET_{mean} (D) for the original PiRadAS.

The non-parametric Wilcoxon statistical test (two paired groups) demonstrated that the rWEPL difference of the original PiRadAS is not statistically equivalent to the analytical simulations characterized by different physical parameters, for both list-mode and integration-mode detector configurations. The investigation about physical parameters shows that smaller σ_{BSS} (i.e., ideal pencil beam) and higher E_p (i.e., straight trajectories) benefit the imaging performances of the integration-mode detector configuration, more than the list-mode detector configuration. The list-mode detector configuration is affected by uncertainties of proton trajectories that depend on the object of interest (i.e., heterogeneities within the object of interest and concavities at the edge of the object of interest) rather than physical parameters. A σ_{BSS} larger than the voxel size strongly affects imaging performances of the integration-mode detector configuration, reaching median values of rWEPL difference that largely double the original PiRadAS. The investigation about geometrical parameters is performed with respect to the Nyquist sampling condition, which expresses the relation between the size of the angular step $\Delta\theta$ and the number of bins along ρ, N_ρ, as: $\Delta\theta = arctan\left(\frac{1}{N_\rho / 2}\right)$. In particular, an angular step equal to 1° does not fully satisfy the Nyquist sampling condition for 128 bins along ρ. However, halving the angular step to match the Nyquist sampling condition does not lead to a statistically significant improvement. The differences are imputable to additional interpolation inaccuracies introduced by twice the number of angles. Using 256 bins along ρ in combination with the 1° angular step clearly violates the Nyquist sampling condition. However, an improvement approximately doubling the spatial resolution is observable, suggesting that the deviated proton trajectories compensate for an overvalued angular step according to the Nyquist sampling condition. Finally, no statistically significant improvement is observed when doubling the number of angular steps N_θ.

For the following investigations on proton statistics, the original PiRadAS is taken into consideration. The non-parametric Kruskal-Wallis statistical test (more than two paired groups) demonstrated that in the radiographic domain the WET difference is not statistically equivalent to the original PiRadAS for proton statistics less than 3 protons for both the list-mode detector configuration and the integration-mode detector configuration based on WET_{mean}, but solely less than 25 protons for the integration-mode detector configuration based on WET_{max}. In the tomographic domain the rWEPL difference for both list-mode detector configuration and integration-mode detector configuration based on WET_{mean} is statistically equivalent for different proton statistics. Instead, the rWEPL difference for the integration-mode detector configuration based on WET_{max} is not statistically equivalent for proton statistics less than 5 protons.

4. Discussions

This work proposes an analytical simulator (PiRadAS) to benchmark the imaging performances of list-mode and integration-mode detector configurations with proton pencil beam scanning. Typically, realistic acquisitions are obtained with MC simulations by providing the physical characterization of the object of interest. When MC simulations rely on a clinical CT image, look-up-tables for elemental composition of the object of interest are used for different tissue densities. Relying on the look-up-tables, the spatial distribution of rWEPLs is then calculated. Therefore, investigations on imaging methodologies that rely on clinical CT imaging are affected by the inaccuracies of the MLP algorithm in materials non-equivalent to water, thus compromising the available reference (i.e., the calculated spatial distribution of rWEPLs). To avoid these inaccuracies, MC simulations in non-uniform water equivalent materials can be obtained in water by artificially scaling the density for charged particle ionization processes according to the spatial

distribution of rWEPLs. Compared to MC simulations, the PiRadAS traces the proton trajectories in non-uniform water equivalent materials relying on the iCT reference (i.e., the spatial distribution of rWEPLs), thus excluding or controlling the inaccuracies of the MLP algorithm. For this reason, only MCS is modeled and other phenomena like nuclear interactions and range straggling are not taken into account. Indeed, the neglected nuclear interactions prevent the use of the PiRadAS in attenuation iCT imaging [44] but have the same impact on list-mode and integration-mode detector configurations. The proton statistics have to be interpreted as compensated for detection efficiency, proton statistics loss due to nuclear interactions and uncertainties of proton trajectories due to range straggling. In a recently investigated integration-mode detector configuration for carbon ions based on MC simulations, the minimum number of ions per pencil beam enabling the decomposition of the Bragg peak signal is of order one hundred [23].

In this work, the influence of physical and geometrical parameters which are relevant to iRad and iCT imaging is explored independent of the detector technology. It is worth noting that the discretization of the total absorption detector for the integration-mode detector configuration defines the accuracy of the WET components of the WET histogram. The WET histogram defined in this work is based on the maximum integer WET of the iRad reference to optimize the accuracy and robustness compromise of the WET_{max} selection. In the radiographic domain, the integration-mode detector configuration for relatively higher proton statistics offers comparable (based on WET_{mean}) or superior (based on WET_{max}) imaging performances with respect to the list-mode detector configuration. However, the integration-mode detector configuration based on WET_{max} is affected by reduced proton statistics, as the selection of the WET component with the maximum occurrence eludes the straighter proton trajectories. In the tomographic domain the reduction of proton statistics is mitigated by the multitude of projections. Nevertheless, in the tomographic domain imaging performances of the list-mode detector configuration remain superior to that of the integration-mode detector configuration. Therefore, dedicated imaging methodologies that fully exploit the WET histogram of each pencil beam acquired with the integration-mode detector configuration put forward potential advantages of this simple and cost-effective configuration in clinical scenarios. The uncertainties of proton trajectories due to MCS are reduced at higher pencil beam energies. The uncertainties of proton trajectories due to the BSS compromise the imaging performances of the integration-mode detector configuration, but, similarly to the uncertainties of proton trajectories at the edge of the object of interest, affect also the accuracy of the MLP algorithm [43]. Ideally, an infinitesimal BSS is desired. From a geometrical point of view, there is no justification for doubling the number of angular steps N_θ. The Nyquist sampling condition has to be matched with tolerance on the angular step $\Delta\theta$.

The analytical simulator is also applicable to helium and carbon pencil beam scanning, if the MCS model embedded in the MLP algorithm is adjusted accordingly. Finally, the MLP algorithm provided with the MCS model extended to non-uniform water equivalent materials can be used to estimate the proton trajectories when priors about heterogeneities are available such as from the X-ray treatment planning CT.

5. Conclusion

The analytical simulator for proton iRad and iCT is proposed and used to explore and firstly compare imaging performances of list-mode and integration-mode detector configurations with proton pencil beam scanning. This work is a decisivestep towards assessment of the potentialities of the integration-mode detector configuration enabled with decomposition of the Bragg peak signal. The intrinsic inaccuracies of the MLP algorithm affect the imaging performances of the list-mode detector configuration, which nevertheless remains superior to the integration-mode detector configuration in the tomographic domain. For relatively higher proton statistics, comparable or better imaging performances are offered by the integration-mode detector configuration in the radiographic domain. Therefore, the competitiveness in clinical scenarios of the simple and cost-effective integration-mode detector configuration with respect to the originally proposed list-mode detector configuration relies on the full exploitation of the available information, given that the BSS is not larger than the voxel size. For this purpose, dedicated iRad and iCT imaging methodologies for the integration-mode detector configuration are required. The proposed analytical simulator newely establishes a useful simulation environment for the development and testing of such methodologies.

Acknowledgments

Chiara Gianoli, Sebastian Meyer and Katia Parodi acknowledge funding from the Deutsche Forschungsgemeinschaft (DFG) project “Hybrid imaging framework in hadrontherapy for adaptive radiation therapy” (grant # 372393016) and the DFG Cluster of Excellence MAP (Munich-Centre for Advanced Photonics). The authors acknowledge Prof. Paul Bolton for the proofreading of the manuscript, Dr. George Dedes for producing MC simulations in the early stage of the project, MSc Martin Rädler for the constructive discussions about the accuracy of MCS models and MLP algorithm and Prof. Marco Riboldi for sharing ideas on the (future) uses of PiRadAS.

Declarations of interest

None.

Appendix A. Supplementary data

Supplementary data to this article can be found online at https://doi.org/10.1016/j.ejmp.2019.03.002.

References

[1] Durante M, Loeffler JS. Charged particles in radiation oncology. Nat Rev Clin Oncol 2010;7(1):37–43.
[2] Haberer T, Becher W, Schardt D, Kraft G. Magnetic scanning system for heavy ion therapy. Nucl Instrum Methods Phys Res, Sect A 1993;330(1):296–305.
[3] Schaffner B, Pedroni E. The precision of proton range calculations in proton radiotherapy treatment planning: experimental verification of the relation between CT-HU and proton stopping power. Phys Med Biol 1998;43(6):1579.
[4] Yang M, Zhu XR, Park PC, Titt U, Mohan R, Virshup G, et al. Comprehensive analysis of proton range uncertainties related to patient stopping-power-ratio estimation using the stoichiometric calibration. Phys Med Biol 2012;57(13):4095.
[5] Paganetti H. Range uncertainties in proton therapy and the role of Monte Carlo simulations. Phys Med Biol 2012;57(11):R99.
[6] Knopf AC, Lomax A. In vivo proton range verification: a review. Phys Med Biol 2013;58(15):R131.
[7] Cormack AM, Koehler AM. Quantitative proton tomography: preliminary experiments. Phys Med Biol 1976;21(4):560.
[8] Hanson KM. Proton computed tomography. IEEE Trans Nucl Sci 1979;26(1):1635–40.
[9] Sadrozinski HW, Bashkirov V, Keeney B, Johnson LR, Peggs SG, Ross G, et al. Toward proton computed tomography. IEEE Trans Nucl Sci 2004;51(1):3–9.
[10] Parodi K. Heavy ion radiography and tomography. Physica Medica 2014;30(5):539–43.
[11] Poludniowski G, Allinson NM, Evans PM. Proton radiography and tomography with application to proton therapy. British J Radiol 2015;88(1053):20150134.
[12] Johnson RP. Review of medical radiography and tomography with proton beams. Rep Prog Phys 2017;81(1):016701.
[13] Arbor N, Dauvergne D, Dedes G, Létang JM, Parodi K, Quiñones CT, et al. Monte Carlo comparison of x-ray and proton CT for range calculations of proton therapy beams. Phys Med Biol 2015;60(19):7585.
[14] Schneider U, Pedroni E. Proton radiography as a tool for quality control in proton therapy. Med Phys 1995;22(4):353–63.
[15] Muraishi H, Nishimura K, Abe S, Satoh H, Hara S, Hara H, et al. Evaluation of spatial resolution for heavy ion CT system based on the measurement of residual range distribution with HIMAC. IEEE Trans Nucl Sci 2009;56(5):2714–21.
[16] Amaldi U, Bianchi A, Chang YH, Go A, Hajdas W, Malakhov N, et al. Construction, test and operation of a proton range radiography system. Nucl Instrum Methods Phys Res, Sect A 2011;629(1):337–44.
[17] Sadrozinski HW, Johnson RP, Macafee S, Plumb A, Steinberg D, Zatserklyaniy A, et al. Development of a head scanner for proton CT. Nucl Instrum Methods Phys

Res, Sect A 2013;699:205–10.
[18] Scaringella M, Brianzi M, Bruzzi M, Bucciolini M, Carpinelli M, Cirrone GAP, et al. The PRIMA (PRoton IMAging) collaboration: development of a proton computed tomography apparatus. Nucl Instrum Methods Phys Res, Sect A 2013;730:178–83.
[19] Poludniowski G, Allinson NM, Anaxagoras T, Esposito M, Green S, Manolopoulos S, et al. Proton-counting radiography for proton therapy: a proof of principle using CMOS APS technology. Phys Med Biol 2014;59(11):2569.
[20] Presti DL, Bonanno DL, Longhitano F, Bongiovanni DG, Russo GV, Leonora E, et al. Design and characterisation of a real time proton and carbon ion radiography system based on scintillating optical fibres. Physica Med 2016;32(9):1124–34.
[21] Abe S, Nishimura K, Sato H, Muraishi H, Inada T, Tomida T, et al. Heavy ion CT system based on measurement of residual range distribution. 医学物理 2002;22(1):39–47.
[22] Rinaldi I, Brons S, Gordon J, Panse R, Voss B, Jäkel O, et al. Experimental characterization of a prototype detector system for carbon ion radiography and tomography. Phys Med Biol 2013;58(3):413.
[23] Meyer S, Gianoli C, Magallanes L, Kopp B, Tessonnier T, Landry G, et al. Comparative Monte Carlo study on the performance of integration-and list-mode detector configurations for carbon ion computed tomography. Phys Med Biol 2017;62(3):1096.
[24] Krah N, Testa M, Brons S, Jäkel O, Parodi K, Voss B, et al. An advanced image processing method to improve the spatial resolution of ion radiographies. Phys Med Biol 2015;60(21):8525.
[25] Gianoli C, Meyer S, Magallanes L, Dedes G, Landry G, Nijhuis R, et al. Spatial Resolution Enhancement in Integration-Mode Detectors for Proton Radiography and Tomography. Radiother Oncol 2016;118:S46–7.
[26] Gianoli C, Dedes G, Meyer S, Magallanes L, Landry G, Nijhuis R, et al. PO-0909: Merging proton radiographies with treatment planning CT for adaptive radiation therapy. Radiother Oncol 2016;119:S438.
[27] Rescigno R, Bopp C, Rousseau M, Brasse D. A pencil beam approach to proton computed tomography. Med Phys 2015;42(11):6610–24.
[28] Schneider U, Pedroni E. Multiple Coulomb scattering and spatial resolution in proton radiography. Med Phys 1994;21(11):1657–63.
[29] Schulte RW, Penfold SN, Tafas JT, Schubert KE. A maximum likelihood proton path formalism for application in proton computed tomography. Med Phys 2008;35(11):4849–56.
[30] Eyges L. Multiple scattering with energy loss. Phys Rev 1948;74(10):1534.
[31] Gottschalk B. On the scattering power of radiotherapy protons. Med Phys 2010;37(1):352–67.
[32] Erdelyi B. A comprehensive study of the most likely path formalism for proton-computed tomography. Phys Med Biol 2009;54(20):6095.
[33] Collins-Fekete CA, Bär E, Volz L, Bouchard H, Beaulieu L, Seco J. Extension of the Fermi-Eyges most likely path in heterogeneous medium with prior knowledge information. Phys Med Biol 2017;62(24):9207.
[34] Paganelli C, Summers P, Gianoli C, Bellomi M, Baroni G, Riboldi M. A tool for validating MRI-guided strategies: a digital breathing CT/MRI phantom of the abdominal site. Med Biol Eng Compu 2017;55(11):2001–14.
[35] Segars WP, Development and application of the new dynamic Nurbs-based Cardiac-Torso (NCAT) phantom; 2002.
[36] Böhlen TT, Cerutti F, Chin MPW, Fassò A, Ferrari A, Ortega PG, et al. The FLUKA code: developments and challenges for high energy and medical applications. Nucl Data Sheets 2014;120:211–4.
[37] Ferrari A, Sala PR, Fasso A, Ranft J. FLUKA: A multi-particle transport code (Program version 2005) (No. INFN-TC-05-11); 2005.
[38] Penfold S, Censor Y. Techniques in iterative proton CT image reconstruction. Sensing Imaging 2015;16(1):1–21.
[39] Gianoli C, Riboldi M, Fontana G, Kurz C, Parodi K, Baroni G. A sinogram warping strategy for pre-reconstruction 4D PET optimization. Med Biol Eng Compu 2016;54(2–3):535–46.
[40] Samei E, Flynn MJ, Reimann DA. A method for measuring the presampled MTF of digital radiographic systems using an edge test device. Med Phys 1998;25(1):102–13.
[41] Gianoli C, Bauer J, Riboldi M, De Bernardi E, Fattori G, Baselli G, et al. Regional MLEM reconstruction strategy for PET-based treatment verification in ion beam radiotherapy. Phys Med Biol 2014;59(22):6979.
[42] Biegun AK, van Goethem MJ, van der Graaf ER, van Beuzekom M, Koffeman EN, Nakaji T, et al. The optimal balance between quality and efficiency in proton radiography imaging technique at various proton beam energies: a Monte Carlo study. Physica Med 2017;41:141–6.
[43] Rädler M. Noise Reconstruction in Proton Computed Tomography. Master thesis, Department of Medical Physics, Experimental Physics, Ludwig-Maximilians-Universität München, Munich, Germany; 2018.
[44] Quiñones CT, Létang JM, Rit S. Filtered back-projection reconstruction for attenuation proton CT along most likely paths. Phys Med Biol 2016;61(9):3258.